Title

Multifunctional Conjugated Ligand Engineering for Stable and Efficient Perovskite Solar Cells

Journal

Advanced Materials, 33(32)

ISSN

0935-9648

Authors

Ma, Ke

Atapattu, Harindi R

Zhao, Qiuchen

et al.

Publication Date

2021-08-01

DOI

10.1002/adma.202100791

Peer reviewed

Multi-Functional Conjugated Ligand Engineering for Stable and Efficient Perovskite Solar Cells

Ke Ma,[1] Harindi R. Atapattu,[2] Qiuchen Zhao,[3] Yao Gao,[1] Blake P. Finkenauer,[1] Kang Wang,[1] Ke Chen,[3] Aidan H. Coffey,[1] So Min Park,[2] Chenhui Zhu,[4] Libai Huang,[3] Kenneth R. Graham,[2] Jianguo Mei,[3]* Letian Dou[1,5]*

[1] Davidson School of Chemical Engineering, Purdue University, West Lafayette, IN 47907, USA

[2] Department of Chemistry, University of Kentucky, Lexington, KY 40506, USA

[3] Department of Chemistry, Purdue University, West Lafayette, IN 47907, USA

[4] Advanced Light Source, Lawrence Berkeley National Laboratory, Berkeley, CA, USA

[5] Birck Nanotechnology Center, Purdue University, West Lafayette, IN 47907, USA

Email: jgmei@purdue.edu; dou10@purdue.edu

Surface passivation is an effective way to boost the performance of perovskite solar cells. To date, many molecular passivation layers have been applied onto perovskite surfaces to reduce the defect density. However, these molecules are usually electrically insulating, which imposes an energy barrier for charges to tunnel through. Here, we report the use of a π-conjugated semiconducting organic ligand as a multi-functional interface modifier inserted between the light-harvesting perovskite film and the hole transporting layer (HTL). We show that the conjugated ligand can effectively passivate the surface defects, extract holes from the perovskite, significantly tune the work function of the perovskite surface and facilitate charge transfer between the perovskite and HTL. Devices modified with the conjugated ligand exhibit high-quality interfaces with improved hole mobility and reduced interface recombination rates. Even more interesting, we observe an anchoring-effect of the conjugated ligand with ammonium functional group, which suppresses the light-induced phase segregation in mixed-cation mixed-halide perovskite films. Finally, the conjugated ligand layer provides good adhesion to the HTL and prevents Li ion migration from the HTL into the perovskite layer, which significantly improves the device stability. These functions translate into a triple cation perovskite solar cell device with enhanced power conversion efficiency of 22.06% (from 19.94%) with long-term stability over 1000 hours under continuous illumination.

Introduction

Organic-inorganic halide perovskite solar cells (PSCs) have seen a rapid increase in power conversion efficiency (PCE), reaching a certified value of over 25% for laboratory scale devices[1]. Nevertheless, the long-term stability of the PSCs under operational conditions remains a significant hurdle on the road to commercialization[2]. The best performing PSCs employ electron transporting layers (ETLs) and hole transporting layers (HTLs) for efficient photogenerated charge carrier extraction. However, decomposition of perovskites is usually initialized from the interface between perovskites and the charge transporting layers, owing to the high defect density, interface charge accumulation, and ion migration[3,4]. These issues not only leave the perovskite vulnerable to degradation, but also are sources of non-radiative recombination losses in the devices[5,6]. To address these issues, tremendous efforts have been devoted to interface modification in PSCs[5]. Small organic molecules, polymers, inorganic layers, and low-dimensional perovskites have all been applied to the interface to passivate defects, stabilize the surface lattice, tune the surface potential of perovskite, and simultaneously induce physical coverage to enhance stability[7–15]. However, most of the interface modification methods introduce electronically insulating layers, which brings a trade-off between surface passivation and charge transfer. Therefore, the interface modifications have to be carefully controlled to avoid introducing more non-radiative recombination[8,14].

Large conjugated organic ligands, such as oligothiophene, preserve the hydrophobicity that other insulating molecules possess[16]. On the other hand, the semiconducting properties of conjugated ligands are expected to optimize the interfacial energy band structure and reduce the barrier to charge transfer[17–20]. Considering the multiple functionalities of conjugated ligands, here we developed an organic halide salt, 2-(3'",4'-Dimethyl-[2,2':5',2":5",2'"-quaterthiophen]-5-yl)ethan-1-aminium iodide (4Tm), for post-treatment of the perovskite surface to facilitate charge extraction, improve energy band alignment, reduce interface recombination, and stabilize the perovskite lattice. The conjugated ligand capping treatment shows a high degree of tolerance to the capping condition and capping layer thickness. Facilitated by these properties, we report a triple cation perovskite solar cell with a power conversion efficiency of 22.06%. We further show that this multi-functional conjugated ligand helps to suppress phase segregation and inhibits ion migration in the PSCs, thus leading to improved long-term stability.

Design and Formation of 4Tm Capping Layer

The multifunctional capping layer (MCL) constructed with conjugated ligands is illustrated in Fig. 1a. 4Tm is selected as the conjugated ligand to be introduced between perovskite and HTL, due to its suitable highest occupied molecular orbital (HOMO) level (~ -5.3 eV) that serves as a competent material for gradient hole transport (Fig. 1b)[16]. The designed 4Tm molecule also contains an ammonium group which allows it to form strong ionic and hydrogen bonds with the perovskite surface and composes into a densely packed ligand layer, or even two-dimensional (2D) perovskite layer as discussed below. The triple cation perovskite with a composition of $Cs_{0.05}(FA_{0.87}MA_{0.13})_{0.95}Pb(I_{0.87}Br_{0.13})_3$ (referred to as CsFAMA; FA, formamidinium; MA, methylammonium) is used in this study. The MCL is formed simply by spin coating a solution of 4Tm on the perovskite surface. To confirm the successful formation of MCL, water contact angles of pristine CsFAMA and CsFAMA-MCL films were measured. The contact angle increases from 41° for pristine CsFAMA to 90° for CsFAMA-MCL films (inset of Fig. 1c). This observation indicates that the 4Tm ligands pack on CsFAMA surface with good coverage, thus dramatically improving the hydrophobicity of the film. As a proof-of-concept, we used the steady-state photoluminescence (PL) to roughly assess the carrier behavior in CsFAMA films with MCL. The PL peak of CsFAMA at 755nm is significantly quenched upon introducing 4Tm to the surface of CsFAMA (Fig. 1c), indicating a potential type II junction is formed and efficient charge carrier transfer from CsFAMA to the MCL occurs.

The top-view scanning electron microscope (SEM) images in Supplementary Fig. 1 show the morphology of the CsFAMA surface has negligible differences between pristine film and film with MCL, which indicates well-maintained morphology after surface modification process. We then performed x-ray photoemission spectroscopy (XPS) measurements to probe the composition and interactions on CsFAMA surface before and after MCL modification. The appearance of the S 2p signal at 164.8 eV confirmed the existence of 4Tm on perovskite surface (Supplementary Fig. 2). Angle-dependent XPS provides additional insights into the compositions as a function of depth and reveals that the 4Tm is primarily localized at the film surface[21]. The XPS pattern of Pb 4f for CsFAMA contains two main peaks, $4f_{7/2}$ and $4f_{5/2}$, located at 138.6 eV and 143.5 eV, respectively (Supplementary Fig. 3). The slight shift of Pb peaks toward lower energy by *ca*. 0.1 eV reflects the decreased work function of the CsFAMA-MCL film surface, which may partly be

attributed to p-type doping near the perovskite surface[22,23]. The Pb^0 peaks at 137.2 eV and 142.0 eV are suppressed in CsFAMA-MCL sample, which demonstrates the improved stability and decrease in Pb^0 defects on the perovskite surface after MCL modification[24,25]. The halide/Pb atom ratio in pristine CsFAMA and MCL modified samples are estimated by the integrated area of corresponding peaks, summarized in Table S1. The slight increase in halide/Pb atom ratio in CsFAMA-MCL sample could arise from the formation of a reduced dimensionality phase near the CsFAMA surface.

We attempted to probe the surface structure change using UV-vis absorption, X-ray diffraction (XRD) and 2D grazing-incidence wide-angle X-ray scattering (GIWAXS). While the thin surface layer did not introduce a discernable structure change in UV-vis absorption (Supplementary Fig. 4) and XRD patterns (Supplementary Fig. 5), the low dimension phase was evidenced by the GIWAXS patterns (Fig. 1d, e). Compared to the control sample, a weak signal at q_z of 0.20 $Å^{-1}$ for film with MCL indicates the formation of 2D perovskite. Because of the specific molecular design of this conjugated ligand, 4Tm not only anchors to the CsFAMA surface, but also inserts into the perovskite lattice by replacing organic cations, thus eventually leading to the formation of 2D perovskite layers[16]. Interestingly, both mechanisms have been shown to be effective in passivating surface defects or improving interface charge transport for perovskite solar cells[7,9,12]. The formation of 2D perovskite layer can be seen more clearly by extending the reaction time between the 4Tm solution and the perovskite surface (Fig. 1f). For example, a thick but discontinuous 2D layer was observed upon dipping CsFAMA films into a 4Tm solution for ~6 min (Supplementary Fig. 6). Similar PL quenching effect was observed in the film with such discontinuous thick 2D capping layer, which reveals similar carrier extraction behavior. Here, for our spin-coated 4Tm layer, the contact time between the free 4Tm ligands and the perovskite film surface is quite short and there is no evidence that the 2D perovskite layer is continuous. Therefore, we propose that the MCL is a combination of 4Tm molecular layer and thin 2D perovskite $(4Tm)_2PbI_4$ layer, both of which share similar charge carrier extraction properties (Fig. 1a).

Optical and Electronic Properties of Perovskite Films

The time-resolved photoluminescence (TRPL) spectra of CsFAMA films with and without MCL were collected to probe the carrier dynamics in the perovskite films (Fig. 2a). The nearly mono-

exponential decay from pristine CsFAMA film indicates the high quality of the perovskite film. By contrast, the fast-initial decay from the CsFAMA-MCL film is subjected to either the loss of carriers at the interface due to charge extraction to the MCL, or the interface recombination induced by the 4Tm modification process[26]. The second slow decay, which shows similar decay kinetics between pristine CsFAMA and CsFAMA-MCL, could be attributed to the unaltered surface/interface recombination feature with the addition of MCL.

In order to distinguish the contribution of charge extraction processes to the fast-initial decay of PL intensity, we conducted excitation power-dependent steady-state PL and TRPL measurements. PL quenching effects are observed in CsFAMA-MCL film across all different excitation powers (Fig. 2b). The reduced quenching effect upon increasing excitation power, suggests the speed up of radiative recombination and the saturation of extracted charge carrier density. Excitation power-dependent TRPL studies further unveils the underlying carrier behavior. It has been reported that bimolecular recombination process dominates the charge dynamics under high excitation power, while the monomolecular trap-assisted or surface recombination starts to take the role after decreasing excitation powers[27,28]. Therefore, at sufficiently low excitation power, mono-exponential PL decay is usually observed in neat perovskite films, resulting in longer PL lifetime, as illustrated in Fig. 2d[26,29–31]. The PL decay curves of pristine CsFAMA film does not vary considerably with the excitation power with only slight shorter lifetime at highest excitation power, suggesting the selected excitation powers are in the range of identifying the trap-assisted recombination process. On the contrary, the bi-exponential decay in the CsFAMA-MCL films remains to be pronounced and clearly distinguishable even under low excitation power, demonstrating the charge extraction process takes the lead role in the fast-initial decay (Fig. 2c). The slight increase in lifetime and smeared initial decay upon increasing excitation power could be a consequence of charge accumulation at the interface without further extraction from the system[30]. These results confirm that the PL quenching in the CsFAMA-MCL films is indeed from efficient charge extraction but new non-radiative pathways.

In addition, the CsFAMA-MCL film even possess a faster initial PL decay and a longer tail than that of the Spiro-OMeTAD (2,2’,7,7’-tetrakis(N,N-dip-methoxyphenylamine)-9,9’-spirobifluorene) coated perovskite, which serves as a typical HTL (Fig. 2a). The shape of the

decay curve is relevant to the density of charges that can be stored in charge extraction layers and the interface recombination rates[29,30]. Comparing with the interface contact between perovskite and Spiro-OMeTAD, the MCL possesses stronger bonding with the perovskite surface both physically and electronically, that facilitates more efficient charge extraction and reduces interface recombination rate. These properties result in fast charge collection and long lifetime in CsFAMA-MCL/HTL sample.

We further compared the surface electronic structure of CsFAMA and CsFAMA-MCL films by work function (WF) and valence band maximum (VBM) measurements using UV photoelectron spectroscopy (UPS, Fig. 3a)[32]. We observed a 230 meV decrease in the work function with respect to the vacuum level (E_{VAC}), and a 470 meV decrease in the gap between the Fermi energy and VBM after MCL modification. The corresponding energy-level diagrams are schematized in Fig. 3b. This energy level characterization indicates the surface of CsFAMA shifts from n-type to more p-type after MCL modification, which is likely attributable to the combined effect of conjugated ligand-induced energy-level shift and the suppression of Pb^0 species on surface. The p-type perovskite surface is beneficial for promoting charge transfer between perovskite and p-type doped Spiro-OMeTAD[33]. Moreover, the increased VBM of CsFAMA-MCL surface significantly reduces the energetic mismatch between the transport states in Spiro-OMeTAD (-4.97 eV) and the perovskite, which would minimize the hole extraction barrier at HTL/perovskite interface[34].

PV Performance of 4Tm Treated Perovskites

We fabricated n-i-p planar heterojunction perovskite solar cells with an ITO/SnO_2/CsFAMA perovskite/Spiro-OMeTAD/Au architecture. The champion device with MCL achieved a PCE of 22.06%, with an open circuit voltage (V_{OC}) of 1.17V, a short circuit current (J_{SC}) of 23.78 mA/cm^2, and a fill factor (*FF*) of 79.05% (Fig. 4a). No obvious hysteresis is shown in the current density-voltage (*J-V*) curve under reverse and forward scans, indicating good stability induced by MCL. Additionally, the maximum power point (*MPP*) tracking at voltage of 1 V reveals a stable power output, with a stabilized PCE of 21.43% (Supplementary Fig. 4). In contrast, the control device delivered a PCE of 19.94% with a J_{SC} of 22.96 mA/cm^2, an V_{OC} of 1.14V and a *FF* of 75.83%. The J_{SC} values obtained through *J-V* measurements under solar simulator were verified by the external quantum efficiency (*EQE*) spectra (Fig. 4b). The statistical distribution

of PCE values from 50 control devices and 50 devices with MCL modification demonstrates the reproducibility of the performance enhancement associated with the 4Tm surface treatment, especially the enhancement in all photovoltaic parameters including *FF*, J_{SC} and V_{OC} (Fig. 4c, d, e, f).

Unlike other methods using insulating materials for surface modification of perovskite solar cells, we found that the devices with MCL are less sensitive to the capping layer formation condition, such as ligand concentration and reaction time[9,11]. The concentration of 4Tm solution was tuned from 0.1 mg/mL to 0.5 mg/mL. While low concentrations didn't show an obvious impact on device performance, higher concentrations of 4Tm always result in improved device performance without appreciable variation with 4Tm concentration (Supplementary Fig. 8a). Considering the factor of 4Tm's low solubility in non-polar solvents, a concentration of 0.25 mg/mL is selected to achieve reproducible high-performance devices. Similarly, increasing the reaction time of 4Tm on the CsFAMA surface, as described earlier, did not introduce significant barriers for charge transfer (Supplementary Fig. 8b). Instead, an enhancement in PCE was also observed in devices that have been dipped in 4Tm solution for 6 min, implying the unique electronic property of 4Tm capping layer.

The 4Tm ligand is composed of an oligothiophene tail and an ammonium functional group. To further identify how each component contributes to the efficiency enhancement, we fabricated solar cell devices with different thiophene moieties and different head groups. The detailed *J-V* characteristics are shown in Supplementary Fig. 9 and Supplementary Fig. 10. Mono-, bi-, and ter-thiophene are denoted as 1T, 2T and 3T, which have wide bandgaps. Another quaterthiophene with a smaller bandgap and lower lowest unoccupied molecular orbital (LUMO) level than 4Tm is denoted as BTm (Supplementary Fig. 9). No distinct improvement or even decrease of efficiencies of these devices compared with control devices are observed, and we infer these effects as a result of the unfavorable energy alignment that increases interface recombination, which demonstrates the critical role of improved energy alignment achieved with 4Tm ligand[5,35]. On the other side, the ammonium head group on 4Tm ligand is replaced with carbamate (denoted as 4Tm-Boc), which doesn't have the preferential ionic and hydrogen bonds with perovskite surface. Although the 4Tm-Boc coated perovskite film also possesses enhanced charge extraction, as indicated by steady-state PL quenching, the efficiency of the 4Tm-Boc

modified solar cell does not improve (Supplementary Fig. 10). We hypothesize that the densely-packed and well-oriented 4Tm ligands on the perovskite surface help to stabilize the surface lattice, and the hydrophilic head group together with hydrophobic oligothiophene tail forms a bridge between hydrophilic perovskite and hydrophobic HTL materials, thus further improve the interfacial contact in the devices.

Mechanism of Improved Efficiency

We sought to evaluate the dominant mechanism underpinning the efficiency improvement in devices with MCL using a series of characteristic methods. The light-intensity-dependent V_{OC} plot of CsFAMA and CsFAMA-MCL devices implies slightly suppressed non-radiative recombination in CsFAMA-MCL device (Supplementary Fig. 11). To further elucidate the charge transport behavior in the CsFAMA-MCL devices, we performed Space-Charge-Limited-Current (SCLC) measurements on both electron-only devices and hole-only devices to probe the electron and hole mobility in each device. The MCL modification decreased the electron mobility of the cells from 2.3×10^{-2} $cm^2 \cdot s^{-1} \cdot V^{-1}$ to 0.8×10^{-2} $cm^2 \cdot s^{-1} \cdot V^{-1}$, which is ascribed to the electron blocking effect of 4Tm ligand (Fig. 5a). In contrast, the hole mobility in the CsFAMA-MCL devices is about twice that of the CsFAMA device, which suggests the hole transfer between perovskite and HTL is effectively facilitated by 4Tm (Fig. 5b). Fig. 5c shows the Nyquist plots of the CsFAMA and CsFAMA-MCL devices obtained through electrochemical impedance spectrometry (EIS) measurements. The equivalent circuit corresponding to the impedance patterns is shown in Supplementary Fig. 12. The middle frequency zone of the EIS semicircle is dominated by the recombination resistance in high-performance devices, in which the charge transport resistance is negligible[36]. These plots directly demonstrate the increased recombination resistance and reduced recombination rate at the interface in the device with MCL, thus further confirming our hypothesis of a high-quality interface in 4Tm modified devices[19,37,38]. Moreover, the MCL increased the flat-band potential of the perovskite solar cells by 0.01V, as indicated in the Mott-Schottky plots (Fig. 5d). This result is associated with the improvement in V_{OC} of CsFAMA-MCL device compared with CsFAMA device[12,15].

In addition, we also measured the electroluminescence (EL) spectra of both the CsFAMA and CsFAMA-MCL solar cells, operating as light-emitting-diodes. As shown in Fig. 5e and Fig. 5f, the CsFAMA-MCL devices achieved significantly higher luminescence intensity under the same

injection current compared with the CsFAMA devices, owing to the improved interface and efficient charge transfer.

Impact of 4Tm on device stability

The CsFAMA-MCL thin film exhibited stronger water stability and the larger water contact angle, as mentioned earlier (Supplementary Fig. 13). This strong water repelling property is related with the hydrophobic thiophene tail of the 4Tm ligand. The long tail also slows down the air-induced decomposition, as illustrated through the suppression of Pb^0 peaks in XPS (Supplementary Fig. 3). However, besides moisture and air instability, the stimuli such as light and heat are still present issues.

Ion migration is another critical issue that limits the stability of perovskite solar cells and cannot be resolved by encapsulation. Light-induced ion migration will further cause changes in composition and morphology, which create electronic traps in the devices. Phase segregation in mixed halide perovskites is one of the significant consequences of ion migration[39]. Our CsFAMA film has an optical bandgap of 1.62 eV (extracted from EQE spectrum), which is at the higher end of conventional perovskite solar cells with a bandgap of 1.5-1.6 eV. The wider bandgap increases its potential application in tandem solar cells, but compels it to suffer light-induced phase segregation more significantly than narrow bandgap perovskites[39,40]. Here, interestingly, we found that the CsFAMA-MCL thin films exhibit extraordinary stability and suppressed light-induced phase segregation. Time-dependent PL measurements of CsFAMA films were carried out in air during continuous illumination under white light with 1-Sun intensity. For pristine CsFAMA film, the PL peak of perovskite exhibits an obvious red shift within 10 min, which indicates the formation of low bandgap I-rich domains (Fig. 6a). In contrast, the CsFAMA-MCL thin film show a minimal shift in the PL maximum, demonstrating its excellent photostability (Fig. 6b). This phase segregation evolution was also observed in PL images (Supplementary Fig. 14). The time-dependent PL images of pristine CsFAMA film exhibit evolution of heterogeneity upon light illumination, indicating the formation of narrow band-gap domains that serve as a trap for electron and hole and cause PL quenching[41]. The homogenized PL images from CsFAMA-MCL film implies uniformity across the whole film. In addition, charge-discharge experiments also reveal faster discharge processes in CsFAMA-MCL solar cells, further verifying the reduced ion migration in the CsFAMA-MCL film

(Supplementary Fig. 15). The phase segregation of mixed halide perovskite has been reported to be suppressed by removing excess photogenerated electrons and holes with charge extraction[42]. However, for CsFAMA with 4Tm-Boc capping layer which possesses the same charge extraction behavior as 4Tm, we didn't observe such distinct suppression of PL shift as 4Tm salt did (Fig. 6c and Fig. 6d). We thus conclude that the significant lattice stability induced by 4Tm anchoring on perovskite surface lattice is one critical factor of phase segregation suppression.

We carried out long-term stability test of devices under continuous light illumination with 1-sun intensity in an N_2 environment, without temperature control to simulate normal operating conditions. Lithium-doped Spiro-OMeTAD is applied as HTL in the stability tests to further investigate the influence of lithium-dopant migration on the device stability. At open circuit condition, the CsFAMA-MCL device exhibits a stable post burn-in efficiency (Fig. 6e) after 1000 hrs. In contrast, the CsFAMA control device shows a shorter lifetime. The burn-in effect in both control and CsFAMA-MCL devices has been reported in previous works, especially for the devices tested under illumination at open circuit condition, due to the excess charge carriers accumulation[38,43–47]. Cation migration in wide-bandgap perovskites and elevated temperature in chamber without consistent N_2 flow can exaggerate the burn-in phenomena. In addition, it is noted that the *J-V* curve of CsFAMA control device shows an s-kink after long time illumination, which is usually ascribed to the charge extraction barrier at the interface between active layer and charge extraction layer (Supplementary Fig. 16). In contrast, a smooth *J-V* curve is maintained for the CsFAMA-MCL device with small hysteresis even after 1000 hours of continuous illumination. This indicates the well-preserved interface quality during operation. We attribute this excellent photostability to the unique properties of 4Tm including efficient charge extraction, lattice anchoring effect, and bridging effect between perovskite and HTL, which introduce a structurally- and electronically-robust interface.

Discussion

In summary, we have demonstrated the multi-roles of the conjugated ligands, particularly 4Tm, at the perovskite surface in enhancing solar cell efficiency and improving device stability. 4Tm interface treatment can efficiently extract holes, tune the WF and VBM of perovskite surface for significantly improved band alignment, increase hole mobility, reduce the interface recombination rate and stabilize the perovskite lattice and the interface between perovskite and

HTL, simultaneously. As a result of these superior properties, CsFAMA-MCL-based solar cell achieves a high efficiency of 22.06% with good operational stability and suppressed phase segregation. Our strategy provides a practical method of interface modification that is insensitive to the modification process and represents a new path to overcome the challenging problem of including insulating molecules during surface modification. In addition, the tunability of WF and VBM allows the use of a wider range of HTL materials. Further investigation into conjugated ligand design will likely be critical for achieving minimal loss at interfaces and approaching the potential theoretical efficiency of polycrystalline perovskite devices with excellent intrinsic stability.

Materials. All regents were used as received without further purification. Chemicals used include PbI_2 (Sigma-Aldrich), $PbBr_2$ (Sigma-Aldrich), FAI (GreatCell Solar), MABr (GreatCell Solar), CsI (Sigma-Aldrich), 2,2',7,7'-tetrakis[N,N-bis(p-methoxyphenyl) amino]-9,9'-spirobifluorene (Spiro-OMeTAD, Feiming Chemical Limited), 4-tert-butylpyridine (tBP, Sigma-Aldrich), bis(trifluoromethane)sulfonimide lithium salt (Li-TFSI, Sigma-Aldrich), SnO_2 (15% in H2O colloidal dispersion, Alfa Aesar), Chlorobenzene (CB, Sigma-Aldrich), N,N-dimethylformamide (DMF, Sigma-Aldrich), dimethyl sulfoxide (DMSO, Sigma-Aldrich), isopropanol (IPA, Sigma-Aldrich), acetonitrile (AcN, Sigma-Aldrich), and Gold pellets (99.999%, Kurt J. Lesker). 4Tm were synthesized based on our previous report.

Device Fabrication. The ITO substrate was washed with water, acetone, isopropanol sequentially, and then treated with UVO-zone for 30 min before use. The SnO_2 layer was span coated onto the ITO substrate with a SnO_2 nanocrystal suspension (diluted to 1.67% from 15% stock solution) at 3,000 r.p.m. for 35 s and subsequently annealed at 150 °C for 30 min in air. To prepare the CsFAMA precursor solution, the $FAPbI_3$ (100 mg FAI and 324 mg PbI_2) and $MAPbBr_3$ (30 mg MABr and 116 mg $PbBr_2$) were dissolved in 468 µL and 211 µL of DMF/DMSO mixed solvent (v/v 4/1), respectively. After fully dissolved, the final CsFAMA precursor solution was prepared by mixing 468 µL of $FAPbI_3$ solution, 93.6 µL of $MAPbBr_3$ solution, and 28.2 µL of CsI solution (398 mg/mL in DMSO) under stirring at 60 °C for at least 1 hr before using. As fabricated SnO_2 was treated with UVO-zone for 20 min just before the CsFAMA layer deposition, and transferred into glove box for the following process. The perovskite layer was fabricated by spin coating 30 µL of CsFAMA precursor solution on SnO_2

substrate at a speed of 4,000 rpm for 30 s. 150 µL CB was dropped onto the perovskite layer at 20 s as anti-solvent. The as-casted perovskite film was annealed at 150 °C for 1min and 100 °C for 60 min. For the 4Tm modified device, the 4Tm solution in CB/IPA mixed solvent (v/v 95/5) was drop casted on perovskite surface at 5,000 rpm, followed by drying at 100 °C for 2 min. We found that with or without post-annealing after 4Tm deposition, the device performance is not affected, and 2D layer formation can occur without thermal annealing. The quick annealing process is applied for drying the solvent. After the substrate is cooling to room temperature, the Spiro-OMeTAD solution [51.5 mg Spiro-OMeTAD in 600 µL CB with 20.28 µL tBP and 11.73 µL Li-TFSI (520 mg/mL in AcN)] was spun onto the perovskite film as a hole transporting layer. The device was aged in air for 16 hrs before the evaporation of 90 nm Au as top electrode to complete the fabrication.

Perovskite Film Characterization. PL images were collected with Olympus microscope coupled with an X-CITE 120Q UV lamp. The steady-state PL spectra were measured using a SpectraPro HRS-300. TRPL spectra were measured by time correlated single photon counting apparatus (PicoQiant). The excitation source of both measurements was used a picosecond pulsed laser at 447 nm. The absorption spectra were obtained by an Agilent UV-vis-NIR Cary-5000 spectrometer. The thin film XRD patterns were measured with a Rigaku Smart Lab using a Cu Kα source (λ= 1.54056 Å). The water contact angle was measured with Ramé-hart Model 200. GIWAXS measurements were carried out at beamline 7.3.3 at the Advanced Light Source (ALS) at Lawrence Berkeley National Lab utilizing an incoming X-rays of 10 keV and an incident angle at 0.1°. The scattering intensity was recorded with a Pilatus 2M-2D detector. The SEM images were taken using a FEI Teneo VS SEM at 5kV and 0.1 nA using a back-scattered electron detector. The UPS measurements were performed with a H Lyman-α photon source (E-LUX^{TM} 121) with a photon energy of 10.2 eV and a 5.85 eV pass energy while the sample was biased at negative 5 V. The XPS measurements were done with a PHI 5600 ultrahigh vacuum system using a hemispherical electron energy analyzer and an Al Kα source (1486.6 eV, PHI 04-548 dual anode X-ray source)for excitation. Core-level signals were obtained at 0°, 45° and 75° electron take-off angles with a 23.5 eV pass energy.

Device Characterization. *J-V* characteristics were collected with simulated AM1.5G irradiation (100mW/cm^2), produced by a Xenon-lamp-based solar simulator (Enlitech SS-F5-3A). The light

intensity was calibrated with a calibrated Si solar cell from Enlitech. A Keithley 2450 SourceMeter was used for driving the *J-V* measurements. The active area was 0.11 cm^2, defined by the Au electrode deposition mask. A voltage scan was measured from 1.2 V to -0.1 V then back to 1.2 V. Scan rate of 0.17 V/s was used with a voltage step of 20 mV. The devices were measured in both nitrogen environment and ambient air environment and no obvious difference has been observed. The EQE measurements were performed at zero bias on equipment built in-house using a preamplifier and a lock-in amplifier at a chopper frequency of 161 Hz. The measurements were calibrated with a reference UV-enhanced Si (818-UV-L) diode. The light intensity (φ)-dependent V_{OC} property was studied based on the relation $V_{OC} \propto (k_B T/q) \ln \varphi$, where k_B is Boltzmann's constant, T is Kelvin temperature, and q is the elementary charge. The electron and hole mobilities were measured from SCLC characterization based on electron-only (ITO/SnO_2/perovskite/PCBM/BCP/Au) and hole-only (ITO/PEDOT:PSS/perovskite/Spiro/Au) devices. All devices were measured from 0 to +10 V with step size of 0.02 V under dark condition. The electron and hole mobility values of were calculated by fitting the curve using the Mott-Gurney law in Child's regime using the following equation:

$$J = \frac{9\varepsilon_0 \varepsilon_r \mu V^2}{8L^3}$$

Where L is the thickness of perovskite film, ε_r (i.e., 25) is the relative dielectric constant, ε_0 is the vacuum permittivity, μ is the charge mobility, V is the applied voltage, and J is the current density. The EIS characterization was performed in the dark at a frequency range 100 kHz to 100 mHz using a Versa STAT elcctrochemical workstation (Ametek). Complete devices were used for measurement in air. Devices were exposed to a forward bias potentials of 900 mV, close to the maximum power point voltage, on which a sinusoidal perturbation of 20 mV was superimposed. For Mott-Schottky analysis, capacitance-voltage measurements were performed at fixed frequency (10 kHz) on complete devices with a scan from 0 V to 1.4 V. The LED devices characterizations were carried out with a Keithley 2450 source-meter and a 100 mm integrating sphere coupled with a spectrometer (Enli Technology, LQ-100X).

Film and device stability measurement.

The operational stability tests were carried out at open circuit condition for unencapsulated devices under LED light with solar spectrum. The light intensity was adjusted to 100 mW/cm^2. The devices were tested in a glovebox filled with N_2, with no temperature control. The estimated device temperature during the test is around 55°C. *J-V* characteristics were performed over various times to calculate device efficiencies.

Data availability

All data generated or analyzed during this study are included in the published article and its Supplementary Information and Source Data files.

References

1. National Renewable Energy Laboratory. https://www.nrel.gov/pv/assets/pdfs/best-research-cell-efficiencies.20200925.pdf. *Best-Research-Cell Efficiencies* (2020). Available at: https://www.nrel.gov/pv/assets/pdfs/best-research-cell-efficiencies.20200925.pdf.
2. Rong, Y. *et al.* Challenges for commercializing perovskite solar cells. *Science* **361,** eaat8235 (2018).
3. Ni, Z. *et al.* Resolving spatial and energetic distributions of trap states in metal halide perovskite solar cells. *Science* **367,** 1352–1358 (2020).
4. Cho, A.-N. & Park, N.-G. Impact of Interfacial Layers in Perovskite Solar Cells. *ChemSusChem* **10,** 3687–3704 (2017).
5. Luo, D., Su, R., Zhang, W., Gong, Q. & Zhu, R. Minimizing non-radiative recombination losses in perovskite solar cells. *Nat. Rev. Mater.* **5,** 44–60 (2020).
6. Boyd, C. C., Cheacharoen, R., Leijtens, T. & McGehee, M. D. Understanding Degradation Mechanisms and Improving Stability of Perovskite Photovoltaics. *Chem. Rev.* **119,** 3418–3451 (2019).
7. Liu, Y. *et al.* Ultrahydrophobic 3D/2D fluoroarene bilayer-based water-resistant perovskite solar cells with efficiencies exceeding 22%. *Sci. Adv.* **5,** eaaw2543 (2019).
8. Yang, S. *et al.* Stabilizing halide perovskite surfaces for solar cell operation with wide-bandgap lead oxysalts. *Science* **365,** 473–478 (2019).
9. Jiang, Q. *et al.* Surface passivation of perovskite film for efficient solar cells. *Nat.*

Photonics **13,** 460–466 (2019).

10. Wang, R. *et al.* Constructive molecular configurations for surface-defect passivation of perovskite photovoltaics. *Science* **366,** 1509–1513 (2019).
11. Zheng, X. *et al.* Managing grains and interfaces via ligand anchoring enables 22.3%-efficiency inverted perovskite solar cells. *Nat. Energy* **5,** 131–140 (2020).
12. Jung, E. H. *et al.* Efficient, stable and scalable perovskite solar cells using poly(3-hexylthiophene). *Nature* **567,** 511–515 (2019).
13. Wolff, C. M. *et al.* Perfluorinated Self-Assembled Monolayers Enhance the Stability and Efficiency of Inverted Perovskite Solar Cells. *ACS Nano* **14,** 1445–1456 (2020).
14. Li, H. *et al.* Intermolecular π–π Conjugation Self-Assembly to Stabilize Surface Passivation of Highly Efficient Perovskite Solar Cells. *Adv. Mater.* **32,** 1907396 (2020).
15. Zhang, M. *et al.* Reconfiguration of interfacial energy band structure for high-performance inverted structure perovskite solar cells. *Nat. Commun.* **10,** 4593 (2019).
16. Gao, Y. *et al.* Molecular engineering of organic–inorganic hybrid perovskites quantum wells. *Nat. Chem.* **11,** 1151–1157 (2019).
17. Dunlap-Shohl, W. A. *et al.* Tunable internal quantum well alignment in rationally designed oligomer-based perovskite films deposited by resonant infrared matrix-assisted pulsed laser evaporation. *Mater. Horizons* **6,** 1707–1716 (2019).
18. Meng, L. *et al.* Tailored Phase Conversion under Conjugated Polymer Enables Thermally Stable Perovskite Solar Cells with Efficiency Exceeding 21%. *J. Am. Chem. Soc.* **140,** 17255–17262 (2018).
19. Ran, C. *et al.* Conjugated Organic Cations Enable Efficient Self-Healing FASnI3 Solar Cells. *Joule* **3,** 3072–3087 (2019).
20. Lin, Y. *et al.* π-Conjugated Lewis Base: Efficient Trap-Passivation and Charge-Extraction for Hybrid Perovskite Solar Cells. *Adv. Mater.* **29,** 1604545 (2017).
21. Park, S. M., Abtahi, A., Boehm, A. M. & Graham, K. R. Surface Ligands for Methylammonium Lead Iodide Films: Surface Coverage, Energetics, and Photovoltaic Performance. *ACS Energy Lett.* **5,** 799–806 (2020).
22. Jiang, Q. *et al.* Interfacial Molecular Doping of Metal Halide Perovskites for Highly Efficient Solar Cells. *Adv. Mater.* **32,** 2001581 (2020).
23. Chen, P. *et al.* In Situ Growth of 2D Perovskite Capping Layer for Stable and Efficient

Perovskite Solar Cells. *Adv. Funct. Mater.* **28,** 1706923 (2018).

24. Yang, S. *et al.* Tailoring Passivation Molecular Structures for Extremely Small Open-Circuit Voltage Loss in Perovskite Solar Cells. *J. Am. Chem. Soc.* **141,** 5781–5787 (2019).
25. Wu, Z. *et al.* Highly Efficient Perovskite Solar Cells Enabled by Multiple Ligand Passivation. *Adv. Energy Mater.* **10,** 1903696 (2020).
26. Stolterfoht, M. *et al.* Visualization and suppression of interfacial recombination for high-efficiency large-area pin perovskite solar cells. *Nat. Energy* **3,** 847–854 (2018).
27. Peng, J., Chen, Y., Zheng, K., Pullerits, T. & Liang, Z. Insights into charge carrier dynamics in organo-metal halide perovskites: from neat films to solar cells. *Chem. Soc. Rev.* **46,** 5714–5729 (2017).
28. Kim, J. *et al.* Excitation Density Dependent Photoluminescence Quenching and Charge Transfer Efficiencies in Hybrid Perovskite/Organic Semiconductor Bilayers. *Adv. Energy Mater.* **8,** 1802474 (2018).
29. Abdi-Jalebi, M. *et al.* Charge extraction via graded doping of hole transport layers gives highly luminescent and stable metal halide perovskite devices. *Sci. Adv.* **5,** eaav2012 (2019).
30. Kirchartz, T., Márquez, J. A., Stolterfoht, M. & Unold, T. Photoluminescence-Based Characterization of Halide Perovskites for Photovoltaics. *Adv. Energy Mater.* **10,** 1904134 (2020).
31. Abdi-Jalebi, M. *et al.* Maximizing and stabilizing luminescence from halide perovskites with potassium passivation. *Nature* **555,** 497–501 (2018).
32. Philippe, B. *et al.* Valence Level Character in a Mixed Perovskite Material and Determination of the Valence Band Maximum from Photoelectron Spectroscopy: Variation with Photon Energy. *J. Phys. Chem. C* **121,** 26655–26666 (2017).
33. Agresti, A. *et al.* Titanium-carbide MXenes for work function and interface engineering in perovskite solar cells. *Nat. Mater.* **18,** 1228–1234 (2019).
34. Jeong, M. *et al.* Stable perovskite solar cells with efficiency exceeding 24.8% and 0.3-V voltage loss. *Science* **369,** 1615–1620 (2020).
35. Stolterfoht, M. *et al.* The impact of energy alignment and interfacial recombination on the internal and external open-circuit voltage of perovskite solar cells. *Energy Environ. Sci.* **12,** 2778–2788 (2019).

36. Yoo, S.-M. *et al.* An Equivalent Circuit for Perovskite Solar Cell Bridging Sensitized to Thin Film Architectures. *Joule* **3,** 2535–2549 (2019).
37. Wang, H. *et al.* Ligand-Modulated Excess PbI2 Nanosheets for Highly Efficient and Stable Perovskite Solar Cells. *Adv. Mater.* **32,** 2000865 (2020).
38. Zheng, D. *et al.* Simultaneous Bottom-Up Interfacial and Bulk Defect Passivation in Highly Efficient Planar Perovskite Solar Cells using Nonconjugated Small-Molecule Electrolytes. *Adv. Mater.* **31,** 1903239 (2019).
39. Xu, J. *et al.* Triple-halide wide–band gap perovskites with suppressed phase segregation for efficient tandems. *Science* **367,** 1097–1104 (2020).
40. Kim, D. *et al.* Efficient, stable silicon tandem cells enabled by anion-engineered wide-bandgap perovskites. *Science* **368,** 155–160 (2020).
41. Gautam, S. K. *et al.* Reversible Photoinduced Phase Segregation and Origin of Long Carrier Lifetime in Mixed-Halide Perovskite Films. *Adv. Funct. Mater.* **30,** 2002622 (2020).
42. Lin, Y. *et al.* Excess charge-carrier induced instability of hybrid perovskites. *Nat. Commun.* **9,** 4981 (2018).
43. Lin, Y.-H. *et al.* A piperidinium salt stabilizes efficient metal-halide perovskite solar cells. *Science* **369,** 96–102 (2020).
44. Liu, Z. *et al.* A holistic approach to interface stabilization for efficient perovskite solar modules with over 2,000-hour operational stability. *Nat. Energy* **5,** 596–604 (2020).
45. Chen, B. *et al.* Synergistic Effect of Elevated Device Temperature and Excess Charge Carriers on the Rapid Light-Induced Degradation of Perovskite Solar Cells. *Adv. Mater.* **31,** 1902413 (2019).
46. Lee, J.-W. *et al.* 2D perovskite stabilized phase-pure formamidinium perovskite solar cells. *Nat. Commun.* **9,** 3021 (2018).
47. Nie, W. *et al.* Light-activated photocurrent degradation and self-healing in perovskite solar cells. *Nat. Commun.* **7,** 11574 (2016).
48. Endres, J. *et al.* Valence and Conduction Band Densities of States of Metal Halide Perovskites: A Combined Experimental–Theoretical Study. *J. Phys. Chem. Lett.* **7,** 2722–2729 (2016).

Acknowledgements

This work is supported by the US Office of Naval Research (award no. N00014-19-1- 2296 to L.D.; program managers: J. Parker and P. Armistead), the Davidson School of Chemical Engineering, College of Engineering of Purdue University. K. Ma acknowledges the support from the Lillian Gilbreth Postdoctoral Fellowship from College of Engineering of Purdue University. L.H., J.S and S.D acknowledge the support from US Department of Energy, Office of Basic Energy Sciences through award no. DE-SC0016356. The authors thank A. Liang and Z. Wei for help with materials synthesis; B.W. Boudouris for help with electrochemical impedance spectrometry measurements.

Author contributions

L.D. conceived the idea and supervised the project. K.M. and L.D designed the experiments. K.M. fabricated the devices, conducted the characterization and data analysis. H.R.A., S.M.P. and K.R.G. conducted the UV photoelectron spectroscopy and x-ray photoemission spectroscopy measurements. Q.Z. and L.H. carried out the time-resolved photoluminescence measurements and power-dependent photoluminescence measurements. Y.G. carried out the materials synthesis. C.Z. performed grazing-incidence wide-angle X-ray scattering measurements. B.F. took the scanning electron microscope images. K.W. contributed to the light-emitting device measurement. K.C. and J.M. helped the contact angle measurements. L.H., K.R.G. and J.M. provided advice and expertise. K.M. and L.D. wrote the manuscript. All authors discussed the results and revised the manuscript.

Competing interests

The authors declare no competing interests.

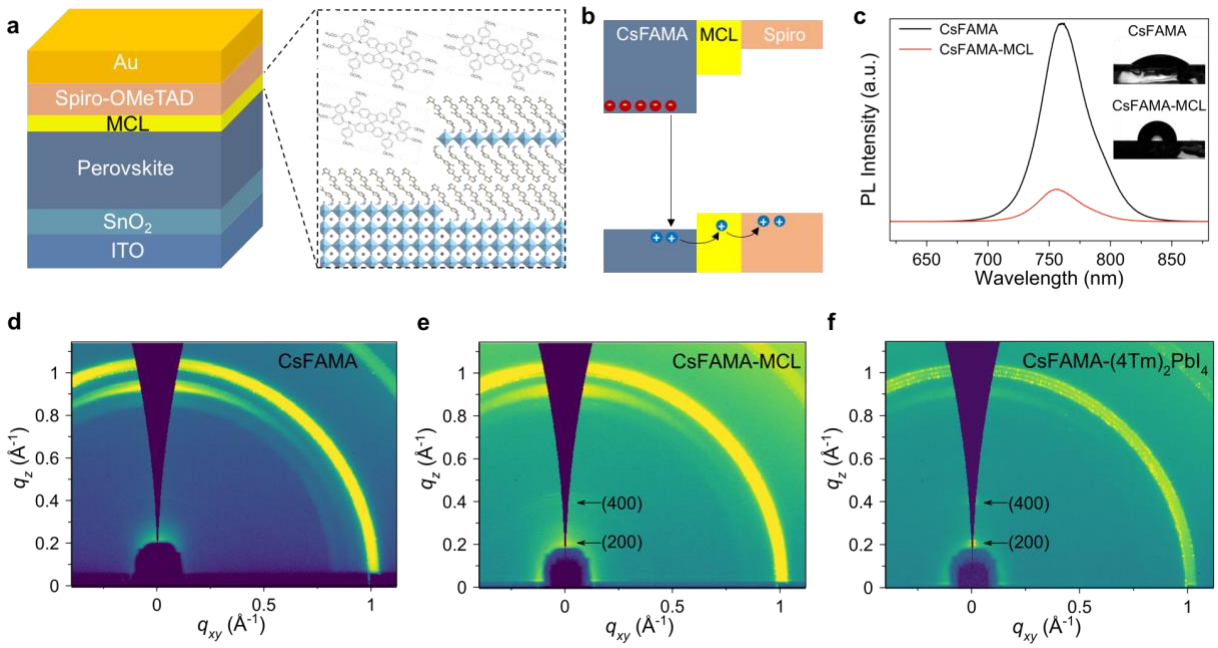

Figure 1| Device structure and surface characterization. a, Left, the structure of a n-i-p perovskite solar cell based on MCL modified interface between perovskite and Spiro-OMeTAD. Right, schematic structure of the MCL structure. **b,** Energy-level scheme and charge transfer direction for CsFAMA device with MCL. **c,** Steady-state PL of CsFAMA films with and without MCL. Inset, the water contact angel of CsFAMA film and CsFAMA-MCL film. **d-f,** GIWAXS patterns of the CsFAMA films without (**d**) and with (**e**) MCL, and the CsFAMA film with thick 2D capping layer (**f**).

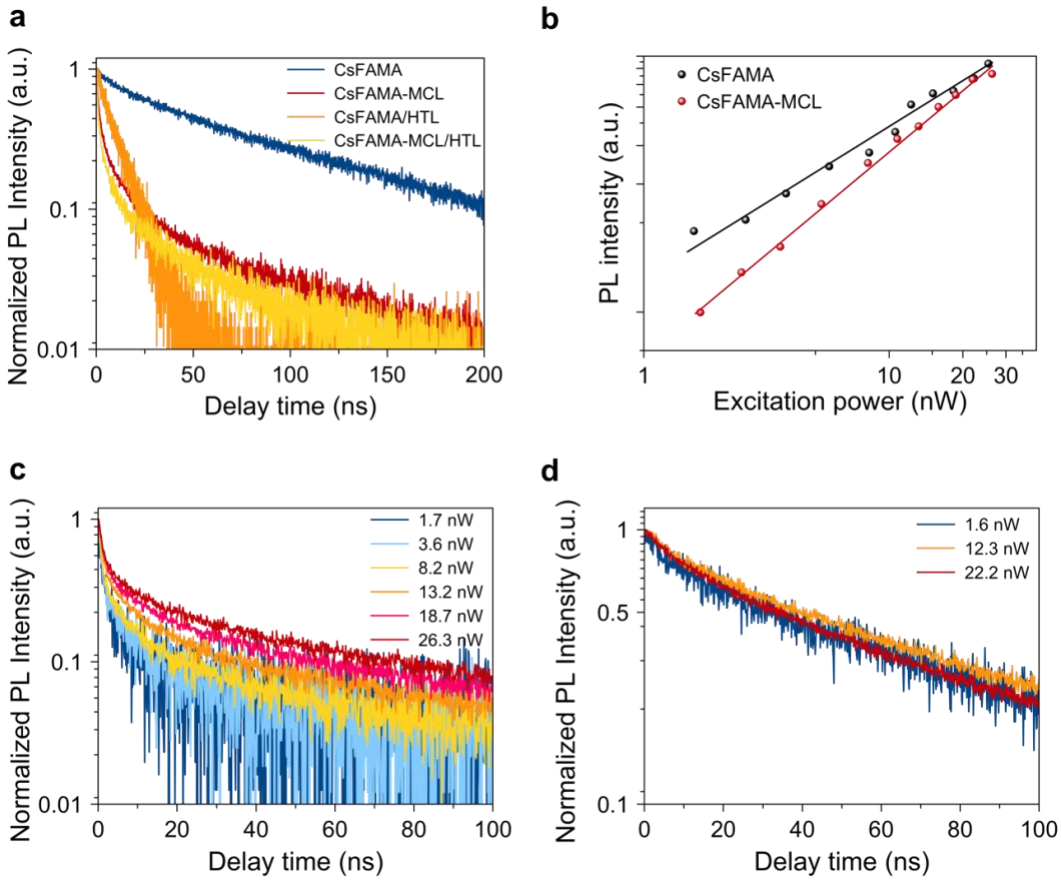

Figure 2| Optical characterization of perovskite films. a, TRPL decay curves for the pristine CsFAMA film, CsFAMA-MCL, Spiro-OMeTAD coated CsFAMA film and Spiro-OMeTAD coated CsFAMA-MCL film. **b**, PL intensities of CsFAMA film and CsFAMA-MCL film, as a function of excitation power. **c,** TRPL decay curves of CsFAMA-MCL films as a function of excitation power. **d**, TRPL decay curves of CsFAMA films as a function of excitation power.

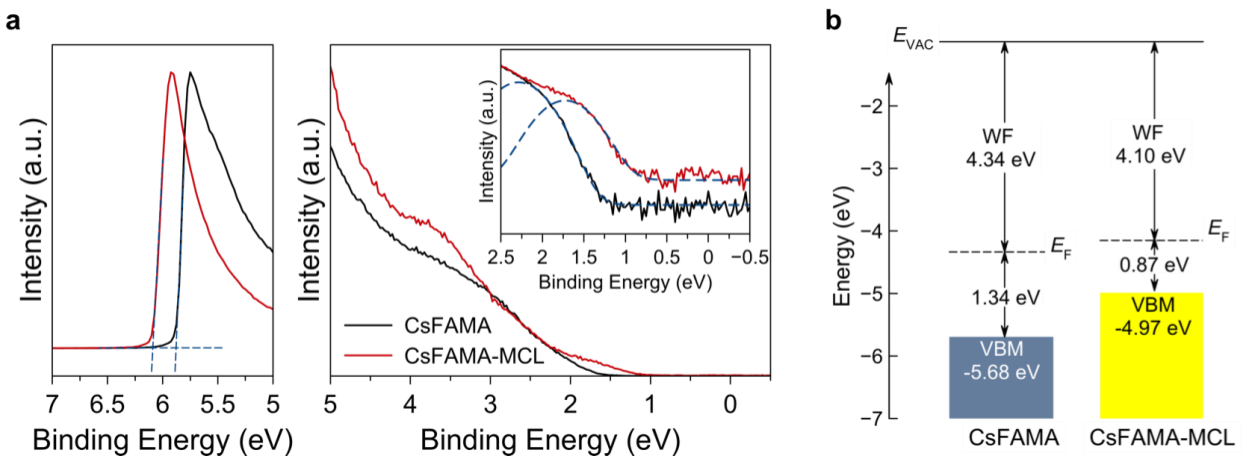

Figure 3| Energy-level characterization of CsFAMA with MCL. a, UPS spectra (using H Lyman-α photon source with a photon energy of 10.2 eV) of the pristine CsFAMA film and film with MCL. The left panel shows the secondary electron cut off region. The right panel shows the UPS spectra in the valence band region, in which the Gaussian fit is used to determine the position of the valence band maximum (VBM) following previous work[21,48]. The VBMs for perovskite surface was determined from semi-log plots. **b,** Energy level scheme of the pristine CsFAMA film and film with MCL based on the parameters derived from UPS.

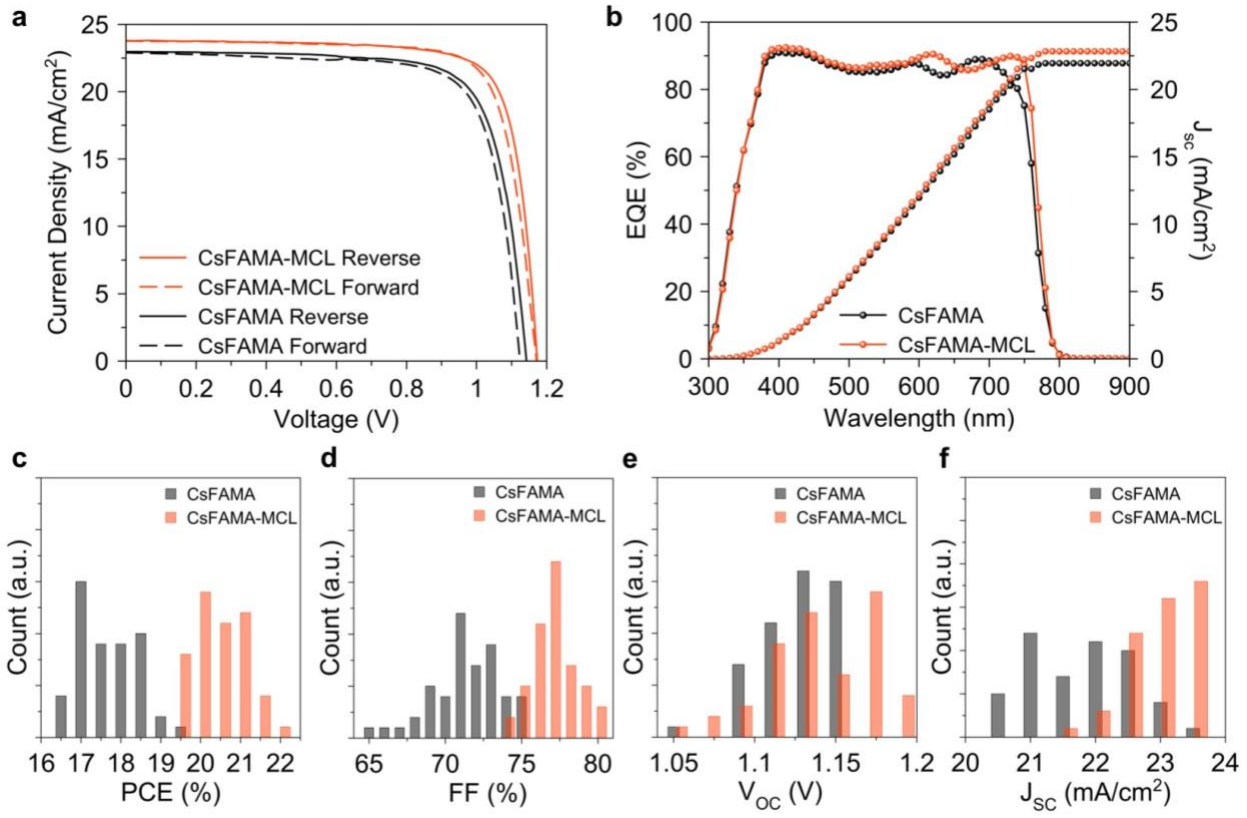

Figure 4| Solar cell device performance analysis. a, *J-V* characteristics of the champion devices based on the CsFAMA and CsFAMA-MCL. **b,** EQE spectra of the champion devices and the integrated photocurrent density, integrated over the AM1.5 (100 mW cm^{-2}) solar spectrum. **c-f,** Histograms showing the PCE **(c)**, *FF* **(d)**, V_{OC} **(e)** and J_{SC} **(f)** values obtained from 50 CsFAMA and 50 CsFAMA-MCL devices.

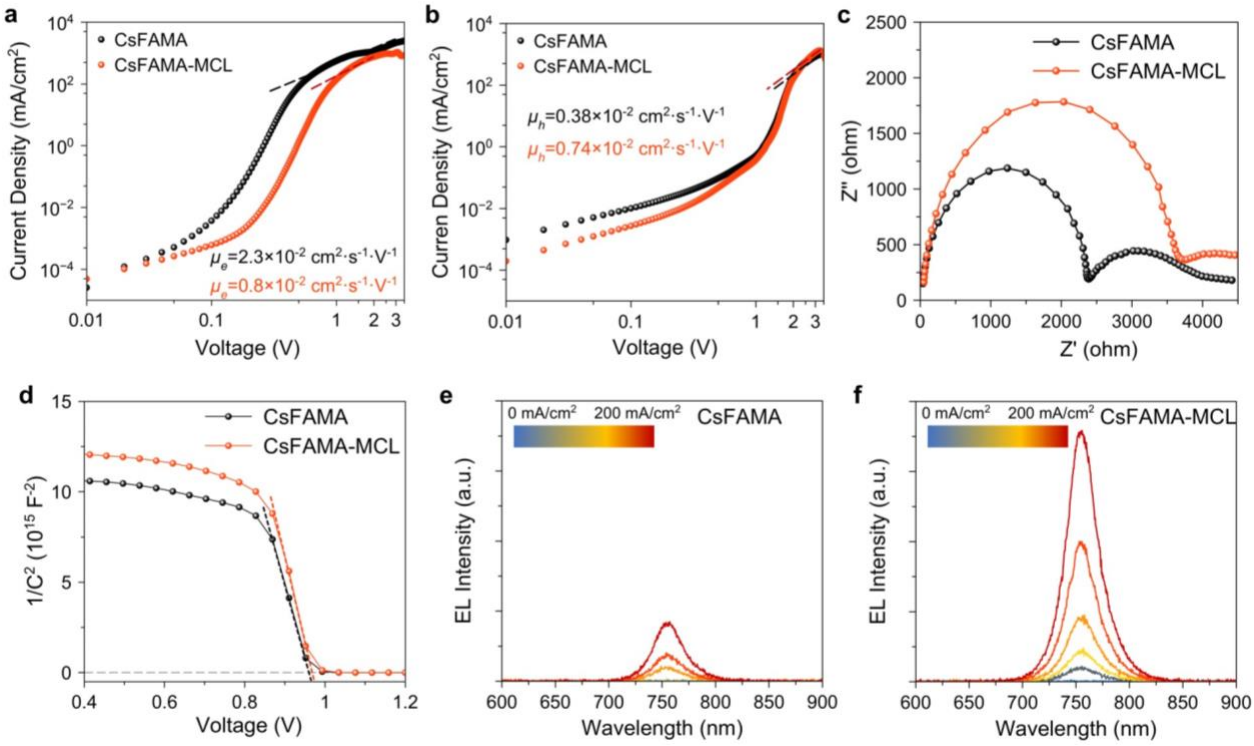

Figure 5| Carrier dynamics analysis of photovoltaic devices. a, Current-Voltage curves of electron-only devices for CsFAMA and CsFAMA-MCL devices. **b,** Current-Voltage curves of hole-only devices for CsFAMA and CsFAMA-MCL devices. **c,** Nyquist plots of CsFAMA and CsFAMA-MCL devices at MPP voltage in the dark, indicating the recombination resistance at interface. **d,** Mott-Schottky plots of CsFAMA and CsFAMA-MCL devices at 5 kHz. **e**, EL spectra of solar cells devices based on CsFAMA under different injection current densities. **f,** EL spectra of solar cells devices based on CsFAMA-MCL under different injection current densities.

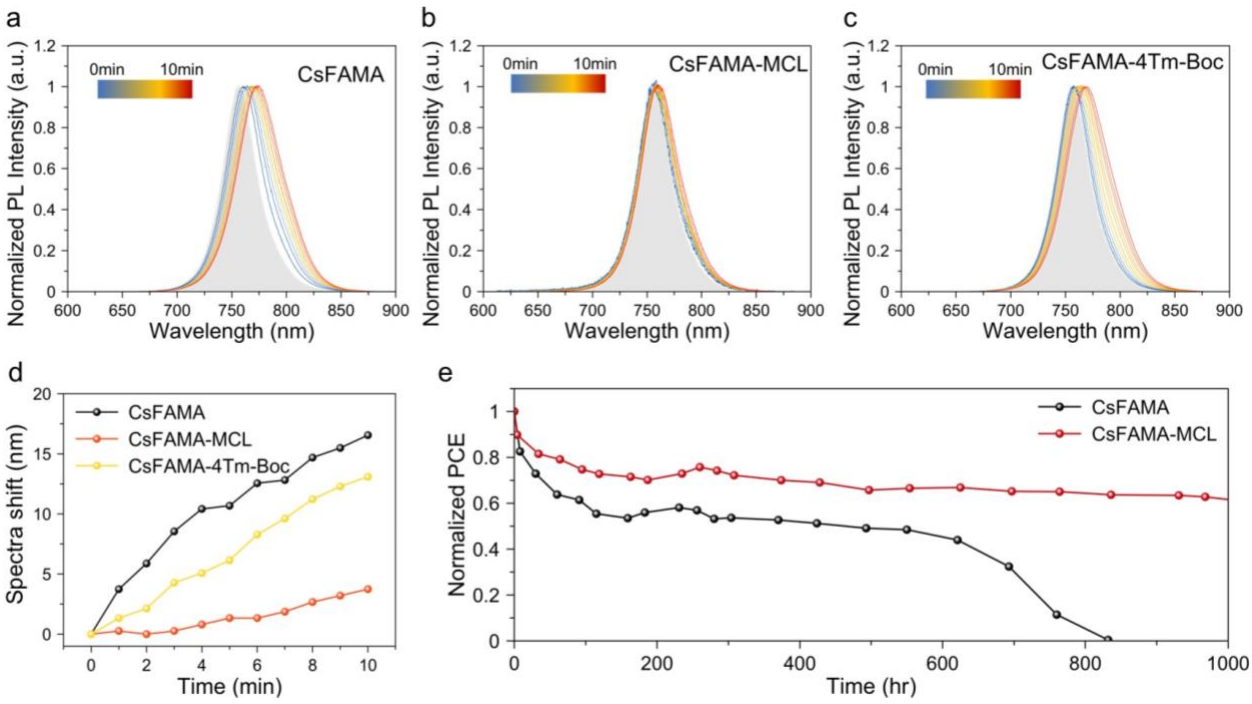

Figure 6| Suppression of photoinduced phase segregation in triple-halide perovskite and long-term stability. a-c, PL spectra of pristine CsFAMA film (**a**), CsFAMA-MCL film (**b**) and CsFAMA film modified with 4Tm-Boc (**c**) under illumination for 10 min. Grey areas indicate the initial PL spectra. **d,** The shift of the spectral centroids of CsFAMA film, CsFAMA-MCL film and 4Tm-Boc modified CsFAMA film over time. **e,** Stability tests of unencapsulated solar cell devices with or without MCL exposed to continuous light (100mW cm^{-2}) under open-circuit condition.